Texture Evolution in Processing of Polystyrene-Clay Nanocomposites

A Thesis

Submitted to the Faculty

of

Drexel University

by

David Richard Steinmetz

in partial fulfillment of the

requirements for the degree

of

Master of Science

July 2007

Dedications

I dedicate this to my parents. Their love and support have made my endeavors possible.

Acknowledgments

I would like to thank my advisors, Dr. Surya Kalidindi and Dr. Christopher Li. Your guidance was invaluable. I would also like to thank Dr. Yossef Elabd for providing guidance and sitting on my committee, and Dr. Patrick Loll for generously allowing me to use his XRD.

Secondly, thank you to the other graduate students who directly helped me with this project: Tony Fast, Kishore Tenneti, Siddhartha Pathak, Aflal Rahmathullah, Ryan VanderMeulen, Stephen Niezgoda, Mike Birnkrant, Matt Hood, Matt Cathell, and Bing Li. Your help was instrumental in bringing this project to fruition.

Lastly, thank you to my parents, family, and close friends for your support. This undertaking was not without challenges, but your constant optimism kept me positive.

Table of Contents

List of Tables

List of Figures

Abstract

Texture Evolution in Processing of Polystyrene-Clay Nanocomposites

David Richard Steinmetz

Surya Kalidindi, Ph.D.; Christopher Li, Ph.D.

Polymers are used in a wide variety of applications, including but not limited to construction plastics materials, electronics and communications, surface coatings, packaging, and automobiles. They are used extensively because they are lightweight, relatively inexpensive, and have desirable properties. A prominent area of interest lies in the enhancement of material properties in polymer systems. The primary method of property enhancement has been the addition of a secondary phase, usually on the nanoscale such as layered silicate clays or carbon nanotubes. The purpose of this study was to develop an innovative technique to study the microstructure of polymer-clay nanocomposites.

An X-ray diffraction technique was developed which allows non-destructive evaluation of orientation distribution of clay plates in polystyrene with two different morphologies: intercalated and phase separated. X-ray diffraction, thermogravimetric analysis, dynamic mechanical analysis, and light absorption were used to characterize the composites.

Observation of texture evolution as a function of strain in polystyrene montmorillonite composites was reported, as was the difference in texture evolution between intercalated and phase separated samples. The difference between texture evolution was also reported using two different diffraction peaks from the same mixed sample, the intercalated peak and the phase separated peak.

Chapter 1: Introduction

Polymers are used in a wide variety of applications, including but not limited to construction plastics materials, electronics and communications, surface coatings, packaging, and automobiles. They are used extensively because they are lightweight, relatively inexpensive, and have desirable properties.

In popular use, polymers refer to plastics. Polymers generally used in commercial applications can have properties that suit the application. Optical clarity, low thermal conductivity, elasticity, and low melting temperatures enabling easy processing are all advantages of polymers for certain uses.

As applications for polymer material systems become more demanding, the desirable properties attained by these material systems alone have begun to become inadequate for new technologies and uses. Therefore, a prominent area of interest lies in the enhancement of material properties in polymer systems. To date, the primary method of property enhancement has been the addition of a secondary phase, usually on the nanoscale such as layered silicate clays or carbon nanotubes. These systems are reported to improve properties such as storage modulus [1], gas permeability [2], thermal stability [3], and flame retardance [3]. Several factors influence the extent of improvement, including the chemistry of the polymer matrix, the structure of the clay or nanotube, the dispersion of nanoclay or nanotube

within the polymer matrix, and the method of preparation.

Currently, these systems are normally only characterized by volume fraction, morphology, and an average description of orientation through orientation factors. The uniaxial Herman's orientation factor has been used, which does not adequately describe a biaxial orientation distribution. White and Spruiell developed a biaxial orientation factor [4] which has also been used [5–7]. This is slightly more robust and provides some insight into the three-dimensional structure, but it still represents an average of orientation of the subject of interest and does not provide a distribution. Bafna et al. take a different approach but only use three XRD images to produce once again an ensemble average of direction cosines used to describe orientation [8].

In order to develop more robust structure-property relationships by more fully understanding the inner workings of a material system, advanced characterization techniques must be developed. It is believed that texture as defined by the orientation distribution of clay plate normals in a polymer-clay nanocomposite is the next important microstructural feature which needs characterization.

An XRD pole figure technique has been used before for semi-crystalline polyethylene [9], blown films of LLDPE/LDPE blends [10], HDPE films [6], uniaxially deformed polyethylene film [7], polyethylene tubes [11], and talc-filled thermoplastics [5]. The talc particles, however, were orders of magnitude larger than the nanoclay particles used in this study (2μm x 0.2μm as opposed to 200nm x 20nm) and they were not intercalated with the polymer matrix. In each of those studies, thin films or drawn fibers were used in reflectance mode or a combination of reflectance and

transmission in order to obtain a complete pole figure.

In many polymer applications, conditions exist which force the processing of composites into sheets or other shapes which produce highly anisotropic properties in the material being processed. These sheets have some deformation history which is linked to the microstructure with anisotropic properties. The proposed technique connects microstructure to properties and is used to describe how microstructure evolves under deformation.

A technique utilizing X-ray diffraction (XRD) is outlined here to characterize polymer-clay nanocomposites by observing texture as defined by nanoclay plate normal distributions. This is an innovation of an existing technique and is the first known presentation of an XRD pole figure analysis of polymer-clay nanocomposites.

Chapter 2: Background

2.1 Orientation Factors

2.1.1 Herman's Orientation Factor

Methods of characterizing the orientation of a polymer have been in use for some time. Herman's orientation function produces a single number that is used to describe the average orientation of a polymer chain. Inherent in the equation is the assumption that this number represents the orientation of each segment of each polymer chain with respect to the axis of interest. Herman's orientation function is thus written as:

$$F_{20}^{j} = \frac{3\langle \cos^2 \phi_{jz} \rangle - 1}{2} \tag{2.1}$$

This equation was originally derived for optical properties but is used for a range of sample characteristics. While F_{20}^{j} can be a rough descriptor of polymer orientation, it does not provide a rich texture analysis of the material system. The value of F_{20}^{j} has the property that if the chain of the polymer is fully aligned with the fiber axis, $F_{20}^{j} = 1$; a random orientation is represented by $F_{20}^{j} = 0$; and when the chain is perpendicular to the fiber axis, $F_{20}^{j} = -0.5$.

It is possible to simplify the initial Euler-based equations into Equation 2.1 and Equation 2.2, called the Nomura/Kawai second moment orientation function when

uniaxial symmetry is assumed.

$$\frac{F_{22}^{j}}{3} = \langle \cos^2 \phi_{jx} \rangle - \langle \cos^2 \phi_{jy} \rangle \tag{2.2}$$

For this second equation, $\frac{F_{22}^{j}}{3} = 0$ represents an isotropic system or uniaxial orientation along z, $\frac{F_{22}^{j}}{3} = 1$ a uniaxial orientation along x, or $\frac{F_{22}^{j}}{3} = -1$ a uniaxial orientation along y. This can characterize uniaxial orientation along any of the three principal directions listed.

Polymer chains may lay at different angles to the fiber axis in crystalline and amorphous regions. The average angle and therefore Herman's orientation factor can be different for different regions of the polymer system. While F_{20}^{j} is traditionally described in relation to the fiber axis, it can be described according to any direction relative to the observer.

Herman's orientation factor and the Nomura/Kawai second moment orientation functions have been used to describe polymer orientation with respect to a fiber axis and carbon nanotube orientation with respect to a fiber axis [12] amongst other things.

2.1.2 White/Spruiell Orientation Factors

Stein and Wilchinsky [13] modified Herman's equations to become descriptors of biaxial orientation. These were subsequently modified by White and Spruiell [4] because they recognized the limitations of Herman's orientation factor: it could only be used to describe uniaxial systems. While this suited some applications, it could not, for instance, describe orientation accurately in a biaxially stretched

polymer film, which has two directions of primary strain. Their equations with respect to the y (machine direction (MD)) and z (transverse direction (TD)) axes take the following form [7]:

$$F_{zj}^{B} = 2\langle \cos^2 \phi_{jz} \rangle + \langle \cos^2 \phi_{jy} \rangle - 1 \tag{2.3}$$

$$F_{yj}^{B} = 2\langle \cos^2 \phi_{jy} \rangle + \langle \cos^2 \phi_{jz} \rangle - 1 \tag{2.4}$$

In this case, $F_{zj}^{B} = 1$ and $F_{yj}^{B} = 0$ represents uniaxial orientation along z, $F_{zj}^{B} = 0$ and $F_{yj}^{B} = 1$ is uniaxial orientation along y, and $F_{zj}^{B} = -1$ and $F_{yj}^{B} = -1$ is uniaxial orientation along x, and lastly $F_{zj}^{B} = 1/2$ and $F_{yj}^{B} = 1/2$ is equal planar biaxial orientation. Equal biaxial orientation states satisfy this condition:

$$\langle \cos^2 \phi_{jz} \rangle = \langle \cos^2 \phi_{jy} \rangle = \frac{\left(1 - \langle \cos^2 \phi_{jx} \rangle\right)}{2} \tag{2.5}$$

2.1.3 Birefringence

Birefringence measurement is also used to gain insight into polymer orientation with respect to an axis of interest. The birefringence can be thought of as a direct measure of the orientation of polymer chains along the fiber axis. An increase in the birefringence value usually indicates a more oriented sample. As with Herman's orientation factor, however, birefringence does little to elucidate the texture of the material and merely provides a path to claim that one sample is "more oriented" than another.

Relations between biaxial orientation factors and birefringence can be developed. Assuming $\triangle^{\circ} = n_c - (n_a + n_b)/2$ and $\delta^{\circ} = n_a - n_b$, refractive indices along the

a, b, and c directions can be obtained:

$$(\Delta n_{MN})_C = 2\Delta^\circ \left(f_{cM} - f_{cN}\right)/3 + \delta^\circ \left(f_{aM} - f_{aN} - f_{bM} + f_{bN}\right)/3 \tag{2.6}$$

$$(\Delta n_{TN})_C = 2\Delta^\circ \left(f_{cT} - f_{cN}\right)/3 + \delta^\circ \left(f_{aT} - f_{aN} - f_{bT} + f_{bN}\right)/3 \tag{2.7}$$

It is further possible to determine the birefringence or orientation factors from the crystalline or amorphous regions [6].

2.2 Polystyrene

Polystyrene is a clear, colorless commodity polymer widely used in automobiles, consumer electronics, insulation, food packaging, and protective packaging. It is used widely in low-cost applications. While it produces significant usable heat when recycled, post-consumer food packaging is not widely recycled due to the cost associated with impurities from the food. However, because of economics, no other post-consumer food packaging material is widely recycled. The major problems with polystyrene are low impact strength and poor chemical resistance. Major producers of polystyrene are Dart Container Corporation, Dolco Packaging, Dow Chemical Company, Genpak Corporation, NOVA Chemicals Corporation, Pactiv Corporation, Prairie Packaging, Sealed Air Corporation - Rigid Packaging Division, TOTAL Petrochemicals USA, Inc., and WinCup.

Polystyrene consists of a carbon backbone saturated with hydrogen, with one hydrogen in each mer unit replaced by an aromatic ring (Figure 1). It forms atactic, syndiotactic, and isotactic varieties, of which the atactic forms a clear, amorphous

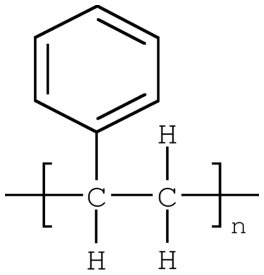

Figure 2.1: Chemical structure of polystyrene

Table 2.1: Properties of polystyrene

Physical Properties	
Density	1.04-1.07 g/cm^3
Mechanical Properties	
Hardness, Rockwell M	70-74
Hardness, Rockwell R	104-120
Ultimate Tensile Strength	17.9-70 MPa
Yield Tensile Strength	25-69 MPa
Elongation at Break	1-45%
Elongation at Yield	1.5-2.2%
Tensile Modulus	1.79-3.38 GPa
Poisson's Ratio	0.33
Thermal Properties	
Linear CTE at 20°C	50-125 μm/m-°C
Thermal Conductivity	0.12-0.193 W/m-K
Glass Transition Temperature	83-100°C
Optical Properties	
Visible Light Transmission	80-90%

structure while the regular periodicity of the syndiotactic and isotactic varieties allow it form discrete crystalline domains from the melt, creating a semicrystalline microstructure. The syndiotactic structure crystallizes several orders of magnitude faster than the isotactic and is important for industrial processes. Syndiotactic and isotactic polystyrene are more expensive than the amorphous atactic structure. A selection of polystyrene's important properties are listed in Table 2.1.

Polystyrene was chosen for this study due to its relatively simply morphol-

ogy. Because it is amorphous, the complexities of semicrystalline polymers are marginalized. X-ray diffraction does not produce sharp peaks possibly interfering with texture measurements, only an amorphous halo indicating the spacing between polymer chains.

2.3 Montmorillonite clay

Montmorillonite (MMT) clay is a member of the phyllosilicate family. It is a naturally-occurring layered silicate similar to talc or mica. It is composed of two tetrahedral silica layers sandwiching an octahedral alumina layer. The silica layers are inward pointing toward the octahedral layer (Figure 2.2).

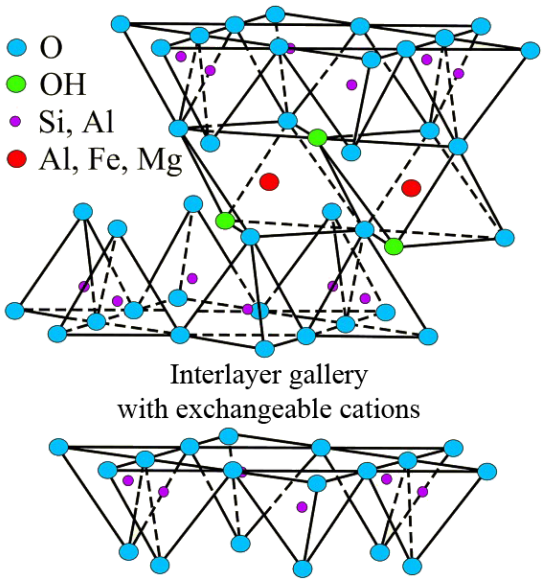

Figure 2.2: The structure of montmorillonite clay

MMT is the most commonly secondary phase in polymer-clay nanocomposites [14] for several reasons. It is cheap and environmentally friendly, available in large quantities, and its intercalation chemistry is well known.

Isomorphous substitution in the clay trilayer can lead to several different vari-

eties of phyllosilicates. That is how the classes of phyllosilicates are differentiated. Based on the level and nature of the isomorphous substitution, the overall charge and density of the clay trilayer can be tailored. Apart from the small compensating effect of internal substitution, this positive charge deficiency is balanced by sorption of extraneous cations which may or may not be exchangeable [15].

The typical thickness of an MMT trilayer structure is 0.95 nm [14]. Positive cations gathering on the surface of the clay sheets increased the d-spacing in the basal (002) direction to between 1.0-1.3 nm. The existence of positive ions on the surface makes the MMT incompatible with any hydrophobic polymers such as polystyrene. In order to facilitate the mixing of the two species the organophilicity of the clay platelets must be increased. That can be done by exchange of these positive ions with organic cations (alkyl ammonium ions $[CH_3(CH_2)_{n-1}NH^3]^+$) where n = 6, 8, 10, 12, 14, 16, and 18 [16–18].

MMT has a large active surface area of 700-800 m^2/g which equates to about a football field for every 12 g. This large surface area allows a large variety of guest molecules to be intercalated into the layered structure of the clay. The extent of intercalation is once again related to the isomorphous substitution.

Talc, which has a neutral electric charge on its layered structure is non-expanding because of the significant amount of energy required to separate the layers, made up of Van der Waals interactions (16.7 kcal/mol) and electrostatic interactions (6.5 kcal/mol) [15]. For MMT to facilitate intercalation it needs to have a low amount of isomorphous substitution (x~0.26-0.60) to allow an environment suitable to swelling and a high ion exchange capacity (70-100 me/100g). Modified clays

show different spacing for different modifiers based on the number of carbon atoms on the alkyl tails of the modifier [19]. To put in perspective with a surfactant used in this study, the milli-equivalent exchange ratio of Cloisite 30B is ~ 95 mequiv [19].

2.4 Polymer-clay nanocomposites

The incorporation of a low volume fraction of nanoparticulates such as layered silicate clay into polymer material systems has been shown to markedly increase mechanical properties. Several factors influence the extent of improvement, including the chemistry of the polymer matrix, the structure of the clay, the dispersion of nanoclay within the polymer matrix, and the method of preparation.

2.4.1 Dispersion of Nanoclay

Many layered silicate clays, including MMT, are hydrophilic due to the abundance of ions in the galleries between clay layers. The ions occur naturally to offset the negative change in the ceramic matrix which accumulates because of isomorphous substitution of ions in the tetrahedral and octahedral crystalline positions. Hydrophilic polymers, such as polyethylene oxide (PEO), are miscible with the MMT in contrast to hydrophobic polymers, such as polystyrene (PS). In order to incorporate hydrophilic clay into a hydrophobic polymer matrix, organic exchange cations replace ions in the galleries through ion exchange reactions. Primary, secondary, tertiary, or quaternary alkylammonium ions exchanged for Na^+ create an organophilic clay surface [20].

Temperature, geometry of the clay discs, polymer degree of polymerization, and volume fraction of the inorganic component dictate the morphology of the compos-

ite, forming isotropic, nematic, and immiscible phases [21]. When hydrophilic clay and organic polymer combine, a phase separated morphology manifests which has little impact on properties. This phase separated morphology is avoided, opting rather for an isotropic or nematic miscible morphology. An intercalated structure in which the polymer penetrates the clay gallery but does not fully disperse the platelets has been shown to increase properties, though not as significantly as complete exfoliation. Some models predict a nematic phase for the platelets with polymer chains coplanar to the trilayers. Intercalation increases the d-spacing of the clay platelets by around 0.5–1.5 nm, a distance associated with a polymer monolayer [21, 22]. To achieve the greatest property enhancement in polymer-clay nanocomposites (PCN), polymer chains must penetrate between and separate the single clay trilayers so that they no longer interact, creating an exfoliated structure.

2.4.2 Methods of Preparation

Many amorphous polymers such as polystyrene (PS) or polymethyl methacrylate (PMMA) are combined with nanoclays to form composites through the intercalative polymerization. During this process, when the catalyst or reacting site for polymerization lies in the clay gallery, free radical polymerization occurs in the gallery forcing apart the clay layers through the force of the polymerization reaction. These reactions form exfoliated nanocomposites.

Emulsion polymerization is a technique whereby a water soluble free radical initiator and largely water insoluble monomer are added to water. A surfactant is added, creating micelles due to the hydrophilic and hydrophobic nature of the

surfactant end groups. These micelles serve as the meeting place of the radical initiator and the monomer. As polymerization proceeds, the micelles grow via the diffusion of monomer from the aqueous phase. The monomer droplets in the water decrease steadily in size. Once the micelles reach approximately 0.5 m in diameter they are called polymer particles. Later, the monomer droplets completely disappear leaving only the polymer droplets. The polymerization process is terminated when the polymer comes into contact with the radical initiator when it diffuses in from the aqueous phase. Because termination is largely dependent on the concentration of initiator, some polymers which cannot be formed through free radical polymerization due to a high rate of self-termination such as butadiene can be polymerized. Polystyrene-clay nanocomposites have been successfully made by swelling the clay layers with water and intercalating the styrene monomers into the silicate layers via emulsion polymerization.

Melt intercalation mixes polymer and clay together in a molten state. The clay must be organically modified to facilitate proper compatibility with the polymer. One advantage of melt intercalation is that no solvent is used. The organic modifiers in the clay act as a surfactant, simultaneously rendering the clay compatible with the polymer chains while weakening the electrostatic interactions between clay layers through a shielding effect. Larger organic modifiers create more shielding and lead to easier intercalation of polymer chains. As alkylammonium chain length increases, so does the basal plane spacing and the trend towards a homogeneous structure between organic chains and alkali ions on the clay surface [23]. The entropy loss associated with the polymer chains confined within the clay gallery

is offset by the conformational entropy gain of the surfactant molecules as the gallery expands [24]. This offset only occurs up until a critical gallery height. The overall entropy change up until the critical gallery height is essentially zero, so even small intermolecular interactions would be enough to intercalate the polymer in the gallery. Above the critical gallery height, however, the strength of the intermolecular interactions would play a larger role in determining if the clay and polymer will intercalate. The main disadvantage of polymer melt intercalation is the degradation of the organic modifiers in the clay at elevated temperatures. Alkylammonium surfactants begin to decompose near 180°C and can thus cause problems if the operation temperature exceeds this value [25].

Solution intercalation has been known for nearly a century, while melt intercalation of polymer-clay nanocomposites has been much more recent. In solution intercalation, the organically-modified clay (organoclay) and the polymer are dissolved in a common solvent, mixed, and then either precipitated or allowed to dry in vacuum. Melt intercalation has the advantage of not needing an organic solvent, many of which are environmentally unfriendly. In the creation of PS-MMT nanocomposites, a large amount of common solvent, tetrahydrofuran (THF) was used. THF is not environmentally friendly and must be properly disposed. The advantages of solution intercalation, however, are clear. The samples prepared via solution intercalation are predominantly homogeneous and thus lead to better understanding of the intercalation process and the structure of the composites.

2.4.3 Properties

Clay additives reinforce the polymer matrix and improve many mechanical and transport properties. Low clay loadings (~1wt%) in PS showed a decrease of 57% and 15% of H_20 and O_2 permeability, respectively, when compared with bulk PS [26]. An increase in clay loading enhanced barrier properties slightly further. Thermal stability in PS also increases as a result of clay additives. The thermal decomposition of PS moves towards higher temperatures when combined with organically modified nanoclay. Dynamic mechanical analysis (DMA) tests clearly show that with increasing clay loading, the dynamic modulus increased up to 60% over that of pure PS at room temperature at a clay loading of 7.6% [27].

2.5 X-Ray Diffraction

An X-ray is electromagnetic radiation which has an energy between gamma rays (~1 MeV) and ultraviolet radiation (~200 eV). X-ray wavelengths vary between 0.01 and 10 nm. Each X-ray has an energy proportional to its frequency and wavelength. Because the wavelength of X-rays are on the order of the atomic structure of many materials, it provides an excellent technique for microstructural investigation.

Bragg's Law states that the distance between two parallel surfaces can be calculated using the path length difference of waves reflecting from the two surfaces in question. Bragg's Law:

$$n\lambda = 2d\sin(\theta) \tag{2.8}$$

where n is an integer indicating the order of the reflection, λ is the wavelength of incident radiation, d is the interlayer distance, and θ is the angle between the

incident radiation and the scattering planes.

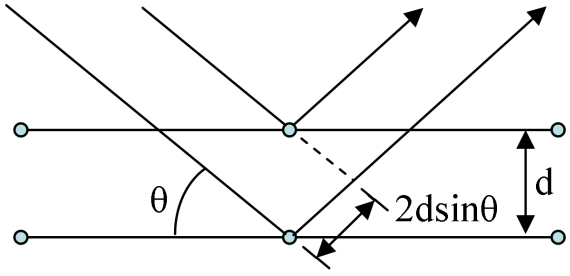

Figure 2.3: Bragg's law illustrating diffraction from a crystalline structure

X-rays are produced in a vacuum tube with two metal electrodes. A tungsten filament cathode is heated and a strong voltage is applied between the electrodes. Electrons leave the cathode and strike a water cooled anode. The resulting deceleration of the electron creates a continuous spectrum of electromagnetic radiation called "Bremsstrahlung". Most of the energy is absorbed by the water, but about 1% is released as X-rays which travel in all directions. X-rays then exit the chamber in which they are created through a Beryllium window, which is highly transparent to them. X-rays strike an image plate and create a pattern in reciprocal space which is indicative of the microstructure of the sample being examined. This technique is used for a wide array of material systems and applications, from protein crystallography to ceramic powder diffraction to fibers.

Chapter 3: Experimental Methods

3.1 Sample Preparation

Polystyrene-montmorillonite (PS-MMT) nanocomposites were made through solution intercalation, which produces homogeneous samples. Polystyrene (PS) [$M_w = 36,000$] and three different types of clay were used: Cloisite 30B, Cloisite 25A, and Cloisite Na+, all produced by Southern Clay Products, Inc. These three clays were chosen because of the differing organic modifiers. The 30B clay has an MT2EtOH (methyl, tallow, bis-2-hydroxyethyl, quaternary ammonium) organic modifier, which is hydrophilic due to the two hydroxyethyl groups, while the 25A clay has an 2MHTL8 (dimethyl, dehydrogenated tallow, 2-ethylhexyl quaternary ammonium) organic modifier which is organophilic due to its lack of highly polar elements. The Na^+ clay is unmodified and thus highly hydrophilic.

Both the polystyrene and the clay were dissolved in a comment solvent, tetrahydrofuran (THF). THF has the chemical formula C_4H_8O and is a ring shape. It is a clear, low-viscosity liquid and has intermediate polarity. It is the fully hydrogenated analog of the compound furan. Its intermediate polarity allows it to readily dissolve both the organic polystyrene and the inorganic MMT. After being placed in the solvent, the PS-THF and MMT-THF solutions were sonicated for 2 hours and then mixed. Subsequently, the mixed solution was sonicated for 12 hours. The solution was precipitated in methanol, filtered using [insert filter paper specs here],

and dried under vacuum for 24 hours.

A given weight was calculated according to the theoretical density of PS and MMT and their respective volume fractions in order to make the prepared samples volumetrically similar. The PS MMT composite was pressed in a Stuers Labopress 3 at 20 kN at 180°C for five minutes and then cooled for five minutes. The resulting discs were 0.7 mm thick. Two rectangular prisms of 0.7x0.7x10 mm^3 were cut from the discs in perpendicular directions and were used to in X-ray diffraction experiments. Both samples were necessary to collect enough data to fill the pole figure.

A sample with a different texture was made by cutting 0.7x2.5x10 mm^3 rectangular prisms from the compressed discs with a sharp razor. These were then stood on the 0.7x2.5 mm^2 side, with the 2.5x10 mm^2 sides touching one another. A total of 4 prisms were placed side-by-side to fill the width of a 2.6 mm channel die. An Instron tensile and compression testing machine was used to press the samples. Force was applied at 110°C until the crosshead reached the necessary displacement. Heat was applied through a heating jacket surrounding the channel die, regulated by a J-type thermocouple. Cuts analogous to those performed on the previous samples were made. XRD, DMA, and gas permeability measurements were taken.

3.2 X-Ray Diffraction and Pole Figures

X-ray diffraction (XRD) was carried out on a Rigaku R-AXIS 4 X-ray diffractometer. X-rays were produced at 40 kV and 20 mA using a rotating copper anode and

were focused using double pinhole collimation. Helium introduced into the X-ray chamber reduced the formation of radicals and stabilized the beam. CuKα X rays were produced at a constant 1.5418 Å with a beam spot size of 300 μm^2. An attached goniometer had one degree of freedom, allowing the sample to be rotated about an axis perpendicular to the incident beam. The detector is an image plate and was positioned 350 mm from the sample. Image collection time was ten minutes.

X-rays attenuate as they pass through a substance, as determined by the following equation:

$$I = I_0 \exp\left(-\mu_m D_m x\right) \tag{3.1}$$

where I is the intensity; I_0 is the original intensity; μ_m [$cm^2 \cdot g^{-1}$] is the mass absorption coefficient, which is characteristic of the substance and changes with wavelength for a given substance; D_m [$g \cdot cm^{-3}$] is the density; and x [cm] is the thickness of the sample. Because of this behavior, if the path of the beam through the sample varies significantly, the intensity of the exiting beam will also vary. Intensity, however, is also affected by the amount of constructive interference created by the sample, which is directly related to the number of electrons exposed to the X-ray beam. The volume exposed is thus responsible for these aspects of beam intensity.

X-ray diffraction images were corrected for both background scattering and volume attenuation through experimental methods. A background image was taken before the experiment began and was subtracted from the sample image before analysis took place. To account for the volume factor, a pure PS sample

was used. The intensity of the image was collected as the sample was rotated through 360°. The relative intensities of each image, spaced at 5° intervals rotated about the goniometer axis perpendicular to the incident beam, were then used as an adjustment of image intensities for the PS MMT samples.

The sample rotated 5° during the ten minute scan, allowing continuous exposure. The average intensities for each 5° interval were then seen in the collected two-dimensional XRD image. A total of 72 images were collected for each sample, with an entire 360° sample scan taking approximately thirteen hours. This was later reduced to 3 hours and 40 minutes. Image analysis was performed using Matlab. Images were converted from the Rigaku OSC format to a format usable by Matlab with the MOSFLM program, a supported part of the CCP4 software suite. Conversion of a batch of images on a 2.13 GHz Pentium 4 with 2 GB of RAM took approximately twelve minutes.

A novel method for constructing pole figures to describe texture of intercalated polystyrene-montmorillonite nanocomposites was developed. The full width at half maximum (FWHM) of the MMT basal spacing peak was calculated after χ integration for each XRD image. The FWHM and center of the peak was computed using Lorentzian curve-fitting in the Fityk peak-fitting software. This was used to create a template which defined the region of each XRD image to be included in calculations. Radial integration of the edited images provided intensity values which correspond to the angles α and β, two angles in spherical coordinates which describe the direction of the normal to a clay platelet on the unit sphere. The distribution of α and β were plotted as a stereographic projection to form a pole

figure. Because the clay trilayers are treated as transversely isotropic discs, only two angles were necessary to fully describe their orientation. Each group of trilayers has two normals. All normals residing in the southern hemisphere were converted to the equivalent normal in the northern hemisphere prior to pole figure construction. Pole figure calculation and construction took approximately six minutes.

3.3 Dynamic Mechanical Analysis

Dynamic mechanical analysis (DMA) is a technique used to study materials. Two different methods are used one being a forced oscillation and the other a decaying oscillation. The forced oscillation method is most commonly used. A stress is applied to a sample. Both solid samples and melts can be tested using DMA. For solid samples, the stress is normally applied linearly in a tensile deformation. For melts, testing is done via shear.

From the deformation under load, the stiffness and therefore modulus of the sample can be determined. For a viscoelastic material such as the polystyrene used in this test,

DMA was performed on a TA Instruments 2980 Dynamic Mechanical Analyzer. A heating rate of 2°C/min was used over a temperature range of 25-150°C. This temperature range was chosen because the glass transition temperature of PS is ~100°C. Samples were of approximate geometry of 1x8x25 mm^3 and were tested in the tensile mode. Loss and storage modulus were calculated automatically by the software. These calculations are dependent on the sample dimensions input by the user.

3.4 Thermogravimetric Analysis

Thermogravimetric analysis (TGA) was performed on the amorphous polystyrene and the polystyrene-montmorillonite nanocomposites. TGA carefully measures the difference in weight of a sample as a function of temperature. Three accurate measurements are necessary: weight, temperature, and temperature change. TGA can be used to determine degradation temperature for polymers and in the case of composites to determine the actual weight percent of a given additive. Because the clay has a high degradation temperature contrasted with the low degradation temperature (~500°C) of the polystyrene, once the polystyrene has been removed the weight of the clay can be reported.

3.5 Light Absorption

The optical clarity of polymers can play important roles in packaging or optical applications. For instance, if polystyrene composites are to be used in food packaging scenarios, it may be desirable to have nearly total optical clarity in order to see the food inside the packaging.

Testing optical clarity is fairly straightforward. A sample of the polymer-composite is subjected to light encompassing all visible wavelengths. A detector on the opposing side of the sample determines the reception of different wavelengths of light. This is compared to a baseline established by shining the light directly at the detector with no sample present. A percentage of each wavelength of light in the desired range, in this case the visible wavelengths, is then calculated.

Visible light absorption can also be used to determine properties about the

dispersion of nanoparticles in the composite. If more light scattering occurs at lower wavelengths, an estimate of space between particles can be made. In this study, the wavelength range of 400-1000 nm.

Chapter 4: Results and Discussion

4.1 Sample Processing

4.1.1 Morphological Considerations

Sample creation was a major challenge. The original goal was to perform gas permeability, XRD, and DMA experiments on the same sample. The nanocomposites could take three different phase morphologies:

- Phase separated – The clay and polymer do not mix
- Intercalated – Polymer chains extend between clay layer sheets but do not fully separate the sheets from one another
- Exfoliated – Clay sheets are completely separated from one another by polymer chains

A phase separated morphology can actually have a negative impact on a composite's properties and is generally not desired. It would, however, be present in XRD images. The exfoliated morphology is associated with the greatest increase in properties but cannot be seen in XRD images. Normally the X-rays diffract from the basal (001) direction of the clay layers since they are approximately 1 nm apart. When the clay layers are delaminated this peak disappears. The absence of Bragg diffraction peaks in the nanocomposites does not necessarily indicate an exfoliated structure, however. Clay dilution, peak broadening can create the impression that

exfoliation has occurred when it indeed has not [28]. Transmission electron microscopy (TEM) is necessary to confirm an exfoliated structure. For these reasons, an exfoliated structure was not desirable for measuring texture with XRD.

The intercalated structure proved to be the natural selection, offering both improved properties and a way to measure texture. Polystyrene was chosen as the polymer in our material system because of its amorphous structure and lack of complexity. It would not create unwanted Bragg diffractions from semi-crystalline domains, obscuring texture information.

X-ray diffraction studies of amorphous polystyrene and the three nanoclays employed in this study were important in determining the peak of interest. The amorphous halo of the polystyrene covers many of the peaks shown by the montmorillonite. The amorphous halo is caused by the spacing of individual polymer chains, which is on the order of 5 Å. Broad peaks are seen at 2θ ~20°and 2θ ~10°(Figure 4.1).

Because atactic polystyrene is amorphous, no long range order corresponding to small diffraction angles should appear in XRD. This leaves the low-angle region free from PS peaks. The basal plane reflections from montmorillonite fall into this region for the unintercalated or unexfoliated clay. The expansion of the basal spacing in the cases of Cloisite®30B and Cloisite®25A is caused by the alkyl chains on the alkylammonium ions of the organic modifier. The number and length of alkyl chains on the alkylammonium ion has a significant impact on the increase of the clay basal spacing. The 25A modifier contains a tallow group largely comprised

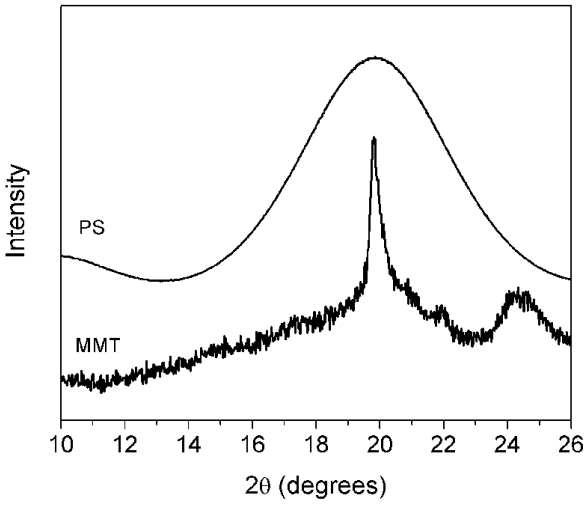

Figure 4.1: XRD scans for polystyrene and montmorillonite clay used in this study

(95%) of C18 and C16 chains with a second C8 chain. Intergallery spacing for modified clay with two alkyl chains was found to be between 1.6 nm for C8 and 2.4 nm for C18 chains[20]. Because there is C18 and one C8 chain in 25A, the basal spacing should be somewhere between the two, which it is (Table 4.1). In fact, this value corresponds well with the C18 spacing for one alkyl chain. The 30B has the same tallow group 95% comprised of C18 and C16 chains. However, the side groups are comprised of only two carbons. Chains of four carbons were shown to have little effect on spacing and thus do not play a role. The basal spacing for 30B modified clay also corresponds to the value for one C18 alkyl group. As polymer chains intercalate between the clay trilayers, this spacing will only increase and will thus produce a diffraction at smaller 2θ values, remaining uninterrupted by the wide amorphous polystyrene peaks.

Table 4.1: Basal plane spacing of montmorillonite

Clay	**2θ**	**Basal spacing**
Cloisite®30B	4.78°	18.5Å
Cloisite®25A	4.75°	18.6Å
Cloisite®Na+	7.56°	11.7Å

4.1.2 Processing

In order to perform three different experiments on the same sample, a number of requirements had to be met. These were complicated by the need to create different textures. The samples must:

- Be thinner than 1 mm
- Be able to be cut into small pieces
- Be intercalated composites
- Be able to be deformed to create different textures

Had only one texture been necessary, sample preparation via a solution casting would probably have sufficed.

First a bulk sample was prepared in a Struers Labopress 3. The sample was cylindrical, 32 mm in diameter and approximately 25 mm in height. The compression axis was perpendicular to the circular face. Slices in the directions parallel and perpendicular to the compression axis were to be made to measure texture. This proved problematic due to the high glass transition temperature of PS. Cutting with a saw damaged the surface of the sample but still marginally worked. The samples were too think to cut with a diamond wire saw.

Microtoming the surfaces of the cut pieces was not possible because of the brittle PS matrix. It flaked and crazed and it was impossible to obtain a thin sample. The thin sample was necessary for XRD and gas permeability. If samples were too thick in XRD experiments, attenuation of the beam can lead to very long collection times. In gas permeability experiments, thicker samples lead to greatly increased measurement times due to the low permeability of the composite. A diamond wire saw and a diamond blade saw were not able to solve this problem. The wire saw was too slow and the diamond blade did not cut samples that were thin enough.

Extrusion was thought to be an option, but several considerations prevented its use:

- The mixing of millimeter sized polystyrene pellets and sub-micron sized nanoclay particles would be problematic without a mixing screw. The polystyrene could be milled to finer sizes but a device in which liquid nitrogen could cool the polystyrene was not available.
- A solution of polystyrene and nanoclay could not be inserted into the extruder because of the lack of a vent for the solvent to evaporate.
- Melt intercalation has been reported to take place near 250°C [29]. Some alkylammonium organic modifiers have been shown to start degradation near 190°C, making melt intercalation a questionable choice.

Finally, 0.7 mm thick samples were able to be created in the same manner as the bulk sample. These thin samples were then cut with a razor blade, producing samples with a consistent geometry.

4.2 Microstructure and Properties

4.2.1 Microstructure

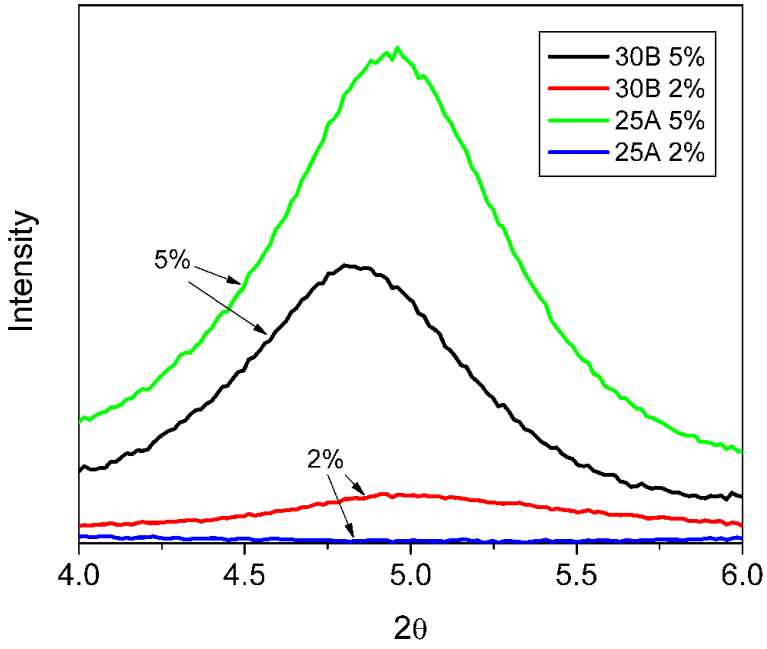

Figure 4.2: Phase separated XRD peak for two montmorillonite clays with two loadings

Once the samples were made, it was necessary to characterize the structure of the nanocomposites. XRD is commonly used to probe the structure of nanocomposites because in intercalated nanocomposites the (001) peak shifts to a lower angle due to the increase in basal spacing caused by the intercalation of polymer between clay layers. There still exist attractive forces between the layers to maintain an ordered structure. XRD can thus successfully be used to determine the extent to which a composite is intercalated or phase separated.

This extends to exfoliated nanocomposites only to a certain extent. The absence of a phase separated or intercalated peak in a nanocomposite can suggest that it is exfoliated, but it has been observed that XRD analysis can lead to false

interpretations of the extent of exfoliation. Clay dilution and peak broadening can cause one to conclude that exfoliation has occurred, and preferred orientation can lead one to conclude that exfoliation has not occurred [30]. For samples suspected of being exfoliated, further TEM studies are necessary to fully characterize the nanocomposite. For phase separated and intercalated structures, however, XRD is enough.

Figure 4.2 shows the XRD peak for phase separated materials. It is clear that the 2wt% samples have a much weaker peak in this region than the 5wt% samples. The peak has primarily shifted to a lower angle because those two composites are mostly intercalated.

A mix of intercalated and phase separated plates are included in the 5wt% nanocomposite samples. Figure 4.3 shows that an intercalated peak exists for all of the samples tested, however because of the existence of a phase separated peak the sample is not homogeneous. Contrary to the 5wt% loading, the samples with a 2wt% loading exhibit an intercalated peak and at most only a very weak phase separated peak or no phase separated peak at all.

4.2.2 Mechanical Properties

Dynamic mechanical analysis (DMA) supported the conclusion that the 2wt% samples were intercalated. The addition of montmorillonite clay to polymers has produced an increase in some mechanical properties such as modulus in many studies, however those studies included intercalated and exfoliated nanocomposites. As shown in Figure 4.4, a decrease in modulus was experienced for all nanocompos-

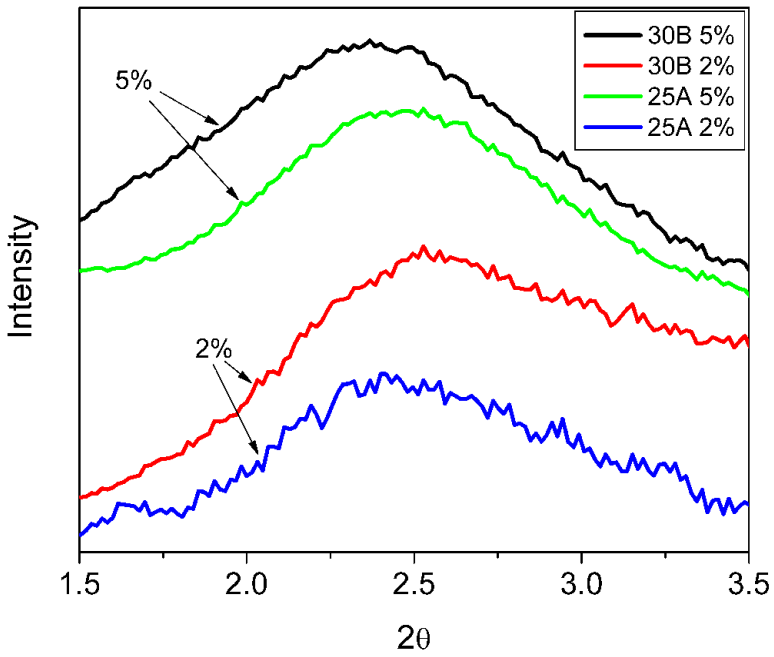

Figure 4.3: Intercalated XRD peak for two montmorillonite clays with two loadings

ites containing a 5wt% MMT loading, as well as the 2wt% Na+ loading. The only two composites that showed an increase in storage modulus were 2wt% 25A and 2wt% 30B. From XRD results, these were the only two thought to be primarily an intercalated structure. Reasons for this could include:

- Instability caused at the polymer-clay interface could make the composite weaker and lower the storage modulus
- The added montmorillonite could act as a plasticizer, increasing the free volume effectively lowering the viscosity and modulus
- The clay layers can slip past one another reasonably well without an intercalating agent. This slip is easier to enact than slipping of tangled polymer chains past one another.

This observation supports the XRD results indicating that only the 2wt% samples are indeed almost fully intercalated.

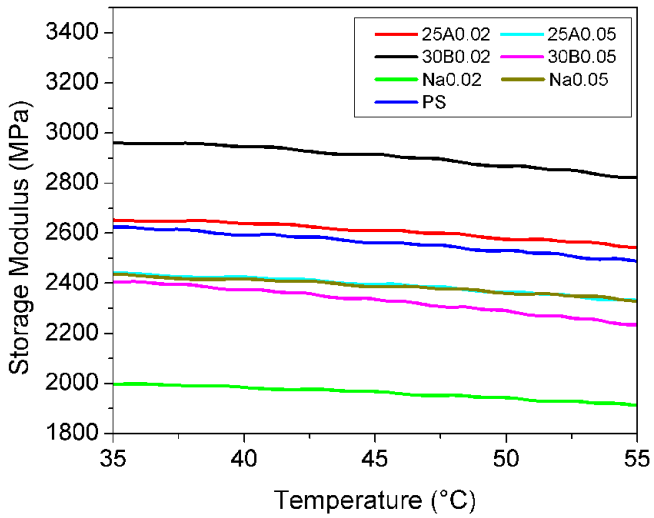

Figure 4.4: DMA results for all tested nanocomposites

4.2.3 Thermal Properties

The thermal stability of all nanocomposites was increased with the addition of nanoclay. The onset of thermal degradation was increased up to 30°C. The final temperature of complete degradation was increased nearly 40°C. The main factor impacting the change in thermal properties is the clay loading. All 5wt% samples show an increase in degradation temperature compared to those with 2wt%. All nanocomposites show an increase compared to the pure PS. Part of each nanocomposite, save the pure Na+, is intercalated, and this is the phase that contributes most significantly to the enhanced thermal properties of the material. The Na+ nanocomposites exhibit increased thermal properties, but they are not as signifi-

cant as 30B or 25A modified clay nanocomposites at the same clay loading. Polymer confinement and attraction to the clay intergallery surface modified with surfactant increases the necessary energy input to commence degradation.

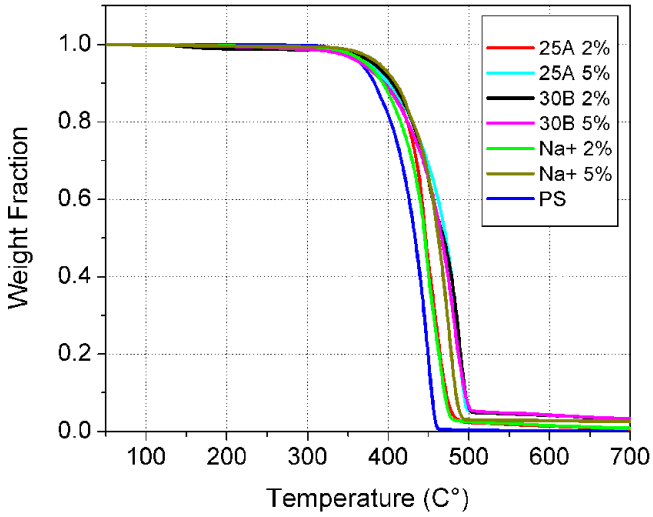

Figure 4.5: Thermal stability measured with TGA

4.2.4 Optical Clarity

Optical clarity was investigated over the range of wavelengths between 400-1000 nm. Pure PS discs had the highest transmittance over the entire range of wavelengths. The next highest transmittance was observed from the 2wt% loaded samples. Lastly, the 5wt% samples displayed the lowest light transmittance in the range observed. Clay modifier tends to not affect the percent transmittance as a whole but rather the overall shape of the curve. For instance, the 25A samples exhibit the same shape and the 2wt% transmits roughly 8-12% more light over the entire wavelength range than the 5wt% sample. The same is true for the 30B

sample, though the 2wt% sample allows only 1-5% more than the 5wt% sample.

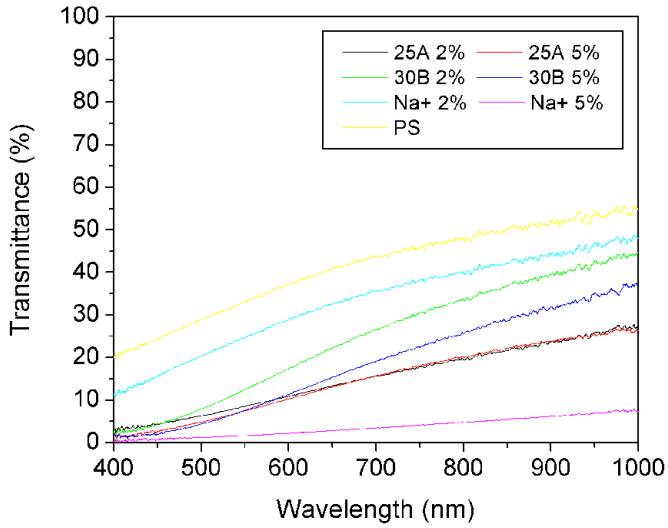

Figure 4.6: Light Transmittance through PS-MMT composites

4.3 Pole Figures

Stereographic pole figures are one method of projecting a three dimensional sphere onto a two dimensional plane. Lines drawn from the southern pole of the sphere end at points on the northern hemisphere. Where these lines intersect the horizontal plane defined by the north-south axis of the sphere is where the orientation defined by each line is projected onto the plane. An illustration is shown in Figure 4.7.

Two angles were defined to describe the orientation of the clay platelets, named alpha and beta. Because the plates are considered transversely isotropic, only two angles are necessary to fully describe their orientation. Alpha was defined as the angle the plate normal forms with the sample rotation axis, which is perpendicular

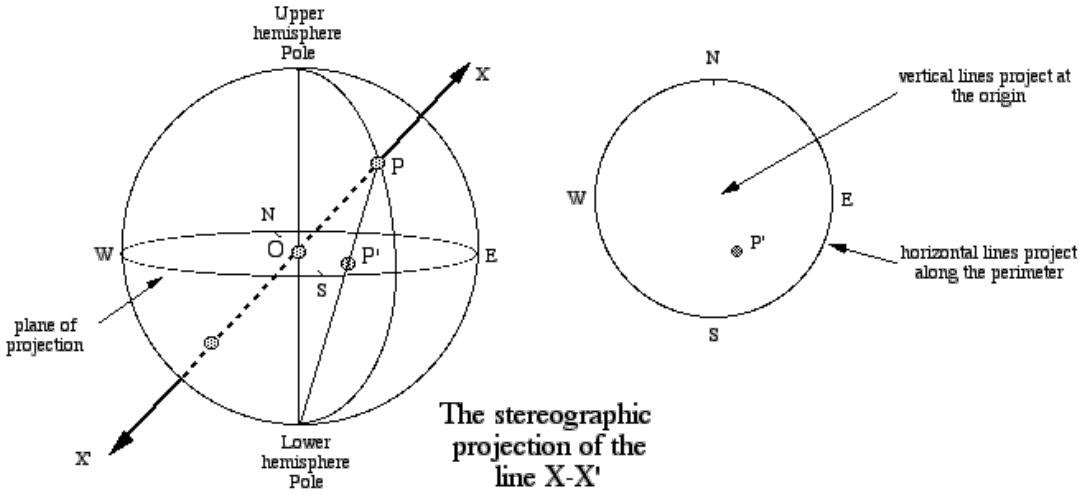

Figure 4.7: Stereographic projection illustrating the projection of a 3D sphere onto a 2D plane [31]

to the incident beam axis. Beta was the angle in the plane defined by the sample rotation axis (rolling direction, RD) and the transverse direction (TD) in the sample coordinate system from the axis parallel to the incident beam (normal direction, ND) at a sample rotation of $\eta = 0°$. A visualization is seen in Figure 4.8.

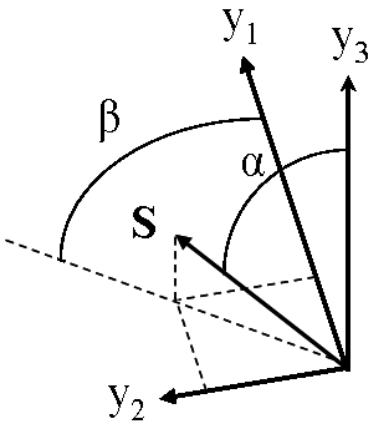

Figure 4.8: Definition of the α and β angles in the sample reference frame. At a sample rotation of 0°: The y_1 direction is the incident X-ray beam axis; the y_2 direction is perpendicular to both the incident beam and the sample rotation axis; the y_3 axis is the sample rotation axis

These two angles were related to the Bragg reflection angle (θ), azimuthal angle (χ), and goniometer rotation angle (η) (Figure 4.9).

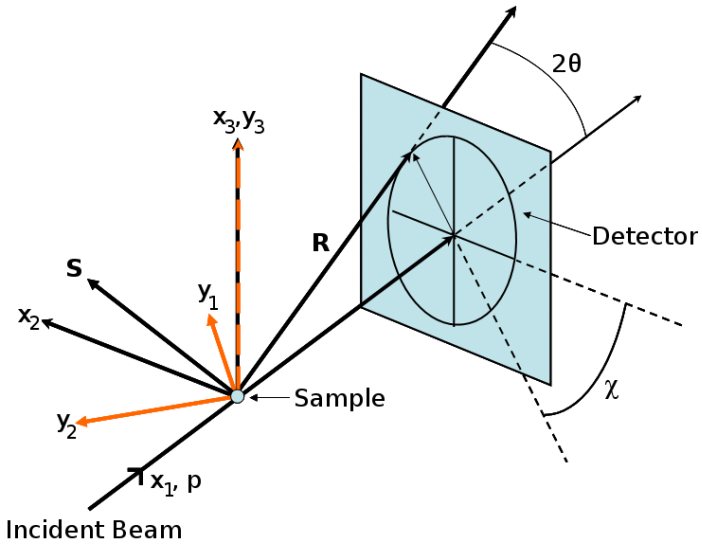

Figure 4.9: Relationships between the Bragg reflection angle (θ), azimuthal angle (χ), and goniometer rotation angle (η) and the plate normal, S

The plate normal, S, was calculated based on the angles θ, χ, and η. The first step to relating these values was to define the incident beam unit vector and determine the reflected beam unit vector in terms of θ, χ, and η *in the diffractometer coordinate system* as shown in Figure 4.9:

$$\mathbf{r}_x = \begin{pmatrix} \cos 2\theta \\ \sin 2\theta \cos \chi \\ \sin 2\theta \sin \chi \end{pmatrix}, \mathbf{p}_x = \begin{pmatrix} 1 \\ 0 \\ 0 \end{pmatrix} \tag{4.1}$$

The vector representing the plate normal, which is not a unit vector, is found by the difference of the incident beam unit vector, **p**, and the reflected beam unit vector, **r**. Before normalization, **S** is:

$$\mathbf{S} = \mathbf{r}_x - \mathbf{p}_x \tag{4.2}$$

$$\mathbf{S} = \begin{pmatrix} -2\sin^2\theta \\ 2\sin\theta\cos\theta\cos\chi \\ 2\sin\theta\cos\theta\sin\chi \end{pmatrix} \tag{4.3}$$

After normalization, **S** becomes the unit vector **s**.

$$\mathbf{s} = \begin{pmatrix} -\sin\theta \\ \cos\theta\cos\chi \\ \cos\theta\sin\chi \end{pmatrix} \tag{4.4}$$

The same unit vector, **s**, was calculated using simple trigonometric relations in terms of the pole figure angles α and β.

$$\mathbf{s} = \begin{pmatrix} \sin\alpha\cos\beta \\ \sin\alpha\sin\beta \\ \cos\alpha \end{pmatrix} \tag{4.5}$$

The two representations of **s** were then equated

$$\begin{pmatrix} \sin\alpha\cos\beta \\ \sin\alpha\sin\beta \\ \cos\alpha \end{pmatrix} = \begin{pmatrix} -2\sin^2\theta \\ 2\sin\theta\cos\theta\cos\chi \\ 2\sin\theta\cos\theta\sin\chi \end{pmatrix} \tag{4.6}$$

and α and β were represented in terms of θ, η, and χ, as shown in the following equations:

$$\alpha = \cos^{-1}(\cos\theta\sin\chi) \tag{4.7}$$

$$\beta = \tan^{-1}\left(\frac{-\sin\eta\sin\theta + \cos\eta\cos\theta\cos\chi}{-\cos\eta\sin\theta - \sin\eta\cos\theta\cos\chi}\right) \tag{4.8}$$

4.4 Validation of Procedure

4.4.1 Compressed Disc

The compressed cylindrical disc with dimensions of 0.7 mm thick and 32 mm in diameter was expected to have a significant number of its clay plates parallel to the circular surface. Therefore, the plane normals of these plates would be perpendicular to that surface. This was expected to occur because of the high

temperature (180°C) relative to the glass transition temperature of polystyrene, the high pressure (20 kN), and to the small thickness (0.7 mm) that the samples were processed. A small fraction of plates standing perpendicular to the compression axis perhaps might have remained in that position, however most other plates would have been moved to a position perpendicular to the compression axis.

Pole figures created from XRD images of the composite showed that this is indeed the case (Figure 4.10). The hydro- or organophilicity of the clay modifier did not appear to significantly affect the texture of the original compressed disc. The Cloisite®25A modifier is organophilic and tends to intercalate more. The result is that each layer in the clay will not be perfectly aligned with the one on top of or below it. Therefore, slightly more variation in orientational distribution of plate normals is seen (Figure 4.10a).

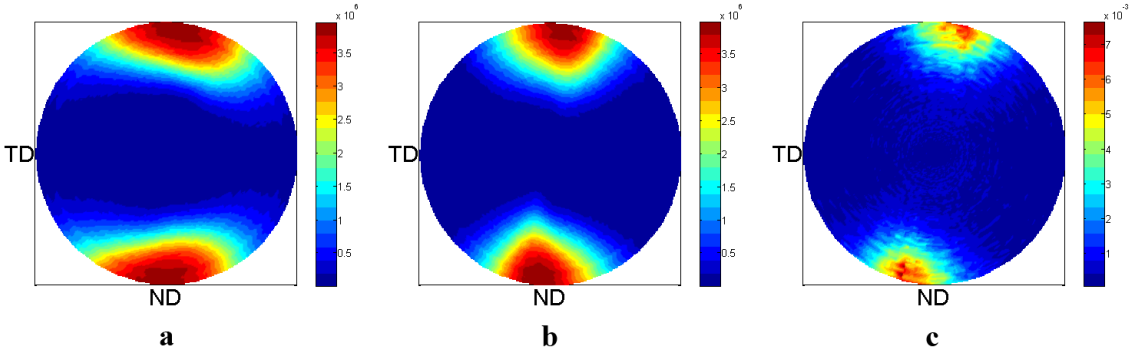

Figure 4.10: Pole figures for the original compressed disc form using three clays. a) 25A b) 30B c) Na+

Concentrations of pole normals can be seen in the $\beta = 0$ and $\beta = \pi$ directions. For the 30B-modified composite (Figure 4.10b), the majority of plane normals are within 30°of the compression axis. This shows a fairly strong preferential orientation. Na+

shows an even stronger orientation preference than the other two clays, owing to its non-intercalation with the polymer.

Pole figures provide more information than an orientation factor. In this case, an orientation factor might provide insight into how close (angularly) the majority of plate normals are to a given axis, but do not tell us where they are. Biaxial orientation factors would point us in the direction in 3D space of the concentration of plate normals but once again not give a clear picture of the total distribution.

4.4.2 Strained Samples

25A - 5wt%

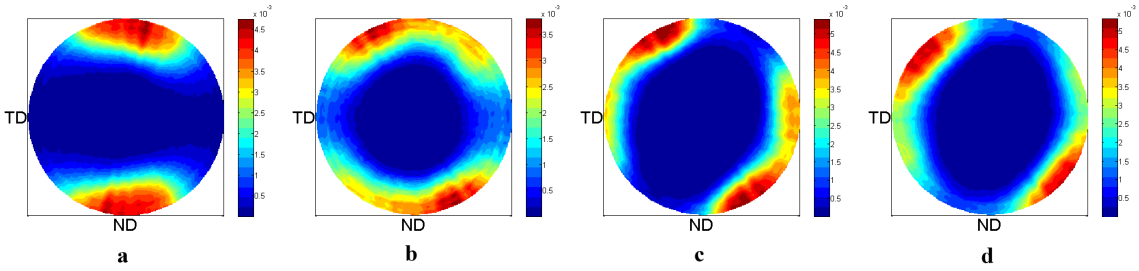

Figure 4.11: Texture evolution as a function of strain for 5wt% 25A. a) The original compressed disc sample, with no strain. Strains of b) 0.32 c) 0.52 and d) 0.60

Strain was induced into samples to modify the microstructure. Different amounts of strain dictated the amount the texture evolved. Texture is presented as pole figures of the clay plate normals.

Strains of 0.32, 0.52, and 0.60, all within ±0.01 mm were imposed upon a sample of 5 wt% 25A organoclay loading. A concentration of the plate normals (poles) is in the direction normal to the original compressed disc as shown in Figure 4.11a. The effective rolling direction, in this case indicating a direction perpendicular to

the compression axis, is at the center of the pole figure. The transverse direction is along the horizontal. The significant features of the pole distribution therefore lie in the normal direction.

Figure 4.11b illustrates the manner in which the plate normals shift as the sample undergoes a finite strain. A halo formed around the outside of the pole figure, indicating a shift from from the normal direction to the transverse direction, which was in plane with the original disc surface perpendicular to the original compression axis. Because the halo does not extend into the center of the pole figure, it is clear that the plate normals are moving in the TD-ND plane, which is also in the plane of the second compression axis. A strain of 0.32 indicates that the area of high concentration of plates has rotated approximately 45 degrees to either side.

The trend continues in Figure 4.11c. While the concentration of plate normals has not moved significantly with the additional strain, the secondary concentration illustrated by the yellow, green, and orange contours has shifted from the ND to the TD.

Finally, in Figure 4.11d, the main concentration of plate normals begins to shift further toward the TD. The secondary halo has shifted slightly farther as well. As strain increases, the main concentration of plate normals leads the shift, remains at a 45 degree while allowing a smaller concentration make their way to the TD before following.

A note has been made that the plates shifted preferentially to one side. This phenomenon is shown later to not be a miscalculation. It could be caused by

buckling in the sample during compression. If the temperature is not high enough, the composite will not ”flow” properly and could cause a preferential distortion of clay plate normals to one side.

This result is significant because these effects could not have been observed without this innovative XRD technique. An orientation factor might have shifted slightly but would not have made known the changes in the halo around the periphery, or that the concentration of plate normals remained in the same place.

30B - 5wt%

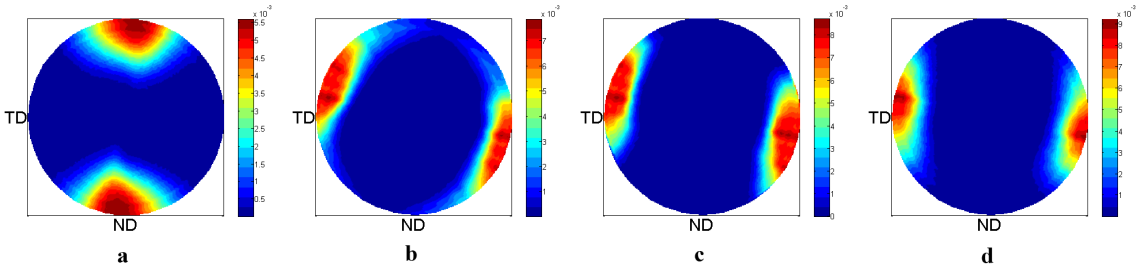

Figure 4.12: Texture evolution as a function of strain for 5wt% 30B. a) The original compressed disc sample, with no strain. Strains of b) 1.5 c) 2.5 and d) 13

As shown in Figure 4.12a and discussed in Section 4.4.1, the original compressed disc sample prepared with 30B has similar characteristics to the 25A sample, with a slightly narrower distribution.

Figure 4.12b has more strain (1.5) than that shown in Figure 4.11d (0.6). It is not surprising then that the sample with higher strain presents a distribution of plate normals that have shifted farther toward TD than the 0.6 strain sample. There is still a slight halo effect in the periphery of the pole figure, indicating that the distribution of clay plate normals is still fairly wide while a majority are concentrated in a given

region.

As the strain increases from 1.5 to 2.5 in Figure 4.12c, the halo disappears and while the main concentration of plate normals does not shift, it becomes much more dense, indicating the shift of the halo to the areas of concentration.

The consolidation of plate normals progresses still further as the strain increases to 13 in Figure 4.12d. The absence of a halo around the periphery, the compaction of the main zone of concentration, and the higher values in the main zone of concentration confirm this fact. The plate normals are still not completely in the TD even with a very high strain, though they are very close. All of this behavior is expected and builds a case for the validation of the XRD pole figure texture analysis technique outlined in this report.

30B - 2wt%

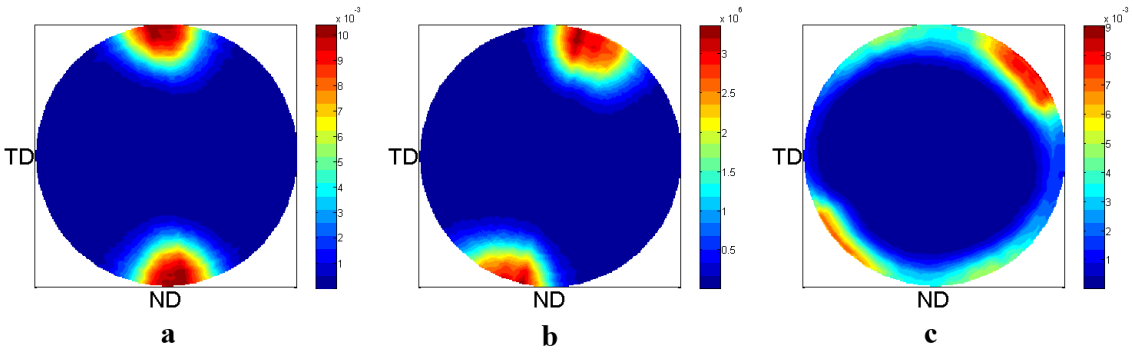

Figure 4.13: Texture evolution as a function of strain for 2wt% 30B. a) The original compressed disc sample, with no strain. Strains of b) 0.06 c) 0.6

The textures of the 2wt% 30B sample, pictured in Figure 4.13, show the same general pattern as in the previous two samples, however there is a notable difference: the 2wt% 30B sample is primarily intercalated. This does not change the

overall behavior of the composite under stain, however, subtle differences are seen. At the small strain of 0.06±0.01, only a very slight shift of plate normal concentration is seen (Figure 4.13b). This is to be expected, since the movement should be less than the sample with 0.32 strain pictured in Figure 4.11b. It is also important to note that the plates are rotating around the pole figure to the right, the opposite of the 5wt% 25A and 30B samples. The calculations of the pole figure are thus proven to be correct, and the coincidental identical rotations of the previous samples were caused by sample asymmetry possibly due to buckling.

The 0.6 strain sample (Figure 4.13c) tells us two things. The first is that the main concentration of plate normals moved approximately the same amount between the TD and ND as the 0.6 strain 5wt% 25A sample. It is promising that equal strain shows equal movement. However, the secondary concentration did not shift in the same manner. In the 0.6 strain 5wt% 25A sample, the secondary concentration has already shifted to the TD, while in the correct sample the secondary concentration remained at the originating ND. A possible, and the probable, cause of this is that the intercalated clay particles are more difficult to shift position because they have polystyrene chains passing between their layers which are entwined in the polystyrene matrix. More strain is then necessary to move the secondary concentration to the TD.

Once again, this result would not have been obtained with orientation factors. They might have indicated that the average angle of incidence with the ND was slightly less than that for Figure 4.11d, but could not have distinguished between the primary concentration and secondary halo.

4.4.3 Sample Heterogeneity

Texture was determined to be more than a function of strain. Heterogeneity in the sample width itself produced different textures. Each of the four segments of the reprocessed specimen was examined for the 5wt% 25A sample. The pole figures of the clay plate normals are shown in Figure 4.14a-d. In Figure 4.14a, the concentration of plate normals is approximately 30-40°from the ND, rotated counterclockwise. This contrasts directly with the concentration of plate normals in Figure 4.14d, which is rotated clockwise from the ND approximately 30-40°. These are the two pieces of the sample which are in contact with the die walls. Friction along the die walls is not an adequate explanation for this phenomenon, however. Fluids move faster and more freely farther from constraining surfaces such as walls. Because of this, it would be expected that the trend would be exactly the opposite of what it is: the left side pole figure being rotated clockwise and the right side pole figure being rotated counterclockwise.

The center two textures, Figure 4.14b-c are intermediates between those on the outside. Figure 4.14b is very similar to the original compressed disc texture, while Figure 4.14c shows a split in both the counterclockwise and clockwise directions, with the clockwise showing a stronger preference.

Figures 4.15a-b show the evolution of texture across an intercalated 2wt% 30B sample. While values are not available for the intermediate sections, the textures in Figure 4.14 suggest that the concentrations of clay plate normals lie along the edge of the pole figure, in the TD-ND plane, between the areas of concentration in

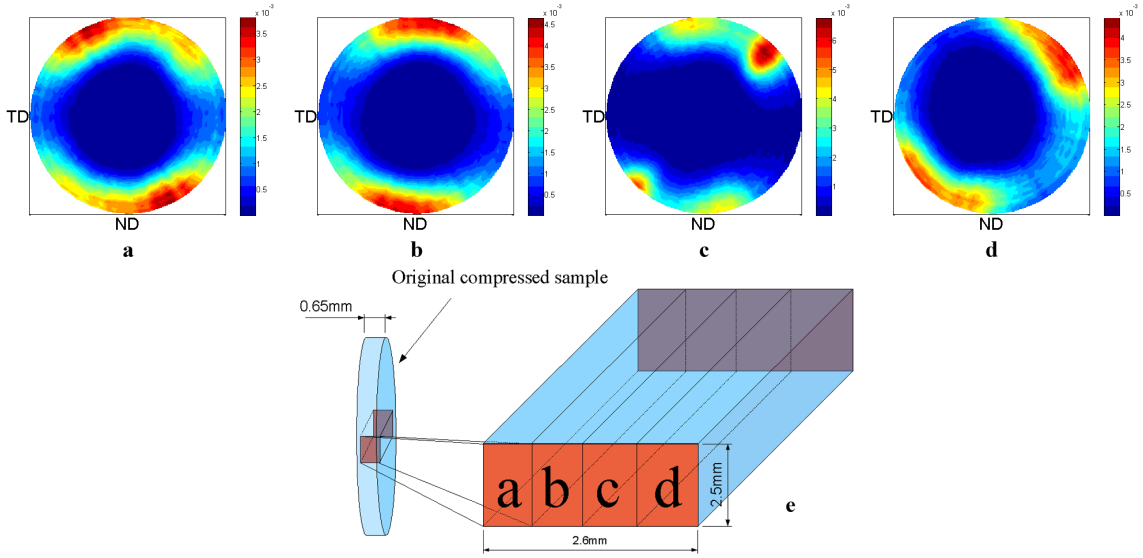

Figure 4.14: Texture evolution across the sample for 5wt% 25A. a, b, c, and d are the pole figures for the corresponding sections in part e, which illustrates how the reprocessed samples were made from the originals. The red faces of the prism are free to move, while the side blue faces are constrained by the die walls and the top and bottom blue faces are constrained by the die floor and the compression fixture.

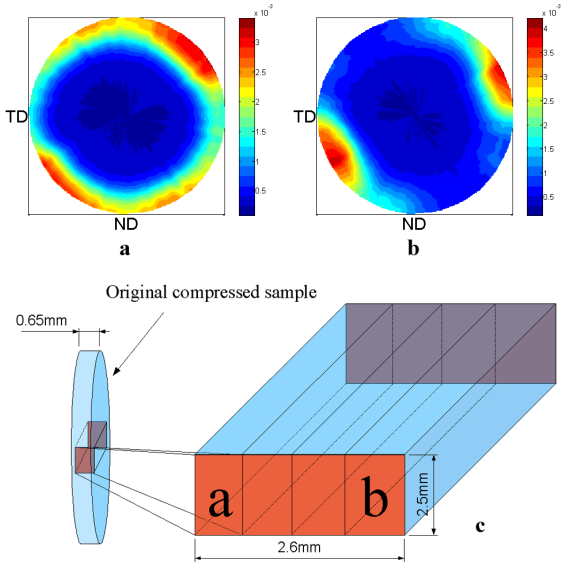

Figure 4.15: Texture evolution across the sample for 2wt% 30B. a and b are the pole figures for the corresponding sections in part c, which illustrates how the reprocessed samples were made from the originals. The red faces of the prism are free to move, while the side blue faces are constrained by the die walls and the top and bottom blue faces are constrained by the die floor and the compression fixture.

the two end textures.

In the intercalated 2wt% 30B sample, it is apparent that the texture does not change drastically from one side of the sample (Figure 4.15a) to the other side of the sample (Figure 4.15). This lends credence to the concept that it is harder to deform the intercalated samples than it is to deform the phase separated ones. Even in the intercalated sample, there are a small number of plates which are still phase separated, as seen from the XRD pattern. If the phase separated particles are indeed easier to move than the intercalated clay particles, the relative lack of motion of the zone of concentration compared to the collection of the secondary concentration around the main zone of concentration fits this description well.

The pole figure for the section on the left, represented as Figure 4.15a, is most similar to that of the primarily phase separated 5wt% 25A sample with a strain of 0.32. It is also similar to the primarily intercalated 2wt% 30B sample with 0.6 strain, however the secondary halo is much stronger in the current sample.

The pole figure for the section on the right, represented as Figure 4.15b, is most similar to that of the primarily phase separated 5wt% 30B sample with a strain of 1.5. If the strain difference is taken to be 0.9, the difference in height of the samples is calculated to be 2.25 mm, which is not possible. All of the samples were 2.5±0.1 mm. Consequently, observations seen in Section 4.4.2 suggest that intercalated clay plates are more difficult to move than phase separated, in which case we could not directly compare the strain-pole figure pair of samples with differing phase morphology.

4.4.4 Effects of Morphology

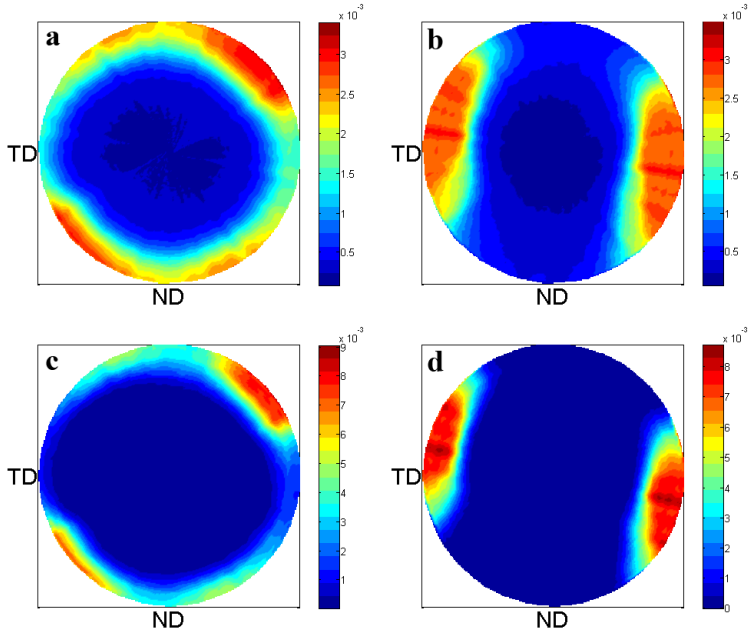

Figure 4.16: The effect of morphology on clay plate normal distribution with different clay loadings. a) 2wt% 30B intercalated b) 5wt% 30B intercalated c) 2wt% 30B phase separated d) 5wt% 30B phase separated

For all of the samples with the exception of the two fully intercalated samples (2wt% 25A and 30B), two XRD peaks exists elucidating the existence of both phase separated and intercalated structures. The intercalated peak is smaller than the phase separated peak in these instances, which indicates a primarily phase separated structure. Both the intercalated peak and phase separated peak can be used to create pole figures, each one describing the texture of the particular phase represented by the peak being used.

Figure 4.16 displays how pole figures change depending on which XRD peak was used to create the pole figure as well as how the pole figures change when the clay loading is increased. The intercalated structures are on the top of Figure 4.16

(a,b), while the phase separated structures are on the bottom (c,d). The two pole figures on the left of Figure 4.16 (a,c) represent 2wt% 30B while those on the right (b,d) represent 5wt% 30B. The 2wt% and 5wt% samples were processed to different strains, resulting in the significantly different textures.

It is clear from the figure that the intercalated peaks produce pole figures describing the texture of the composite system which shows a greater dispersion of clay plate normals than do the phase separated peaks. This again would support the theory that the plates are more difficult to shift from their original position when they have been intercalated by polymer. While the pole figures cannot necessarily determine the dispersion of the particles themselves, the distribution of orientation is wider when the intercalated peaks are used to create the pole figures. For fully intercalated samples, this is obviously the only peak present.

This is a significant effect which would once again not be readily noticeable if orientation factors were the only available means of quantifying texture. The technique used in this study provides a more in depth look into microstructure which can subsequently be used to more fully understand and develop robust structure-property relationships.

Comparison of texture evolution with strain

Figure 4.17 shows texture evolution as a function of strain, calculated using both the phase separated peak (top row) and intercalated peak (bottom row). The differences are clear: the intercalated peak shows a wider dispersion, supporting earlier claims that the intercalated clay particles are more difficult to move from the beginning when they were first compressed and then completely through the

deformation processing.

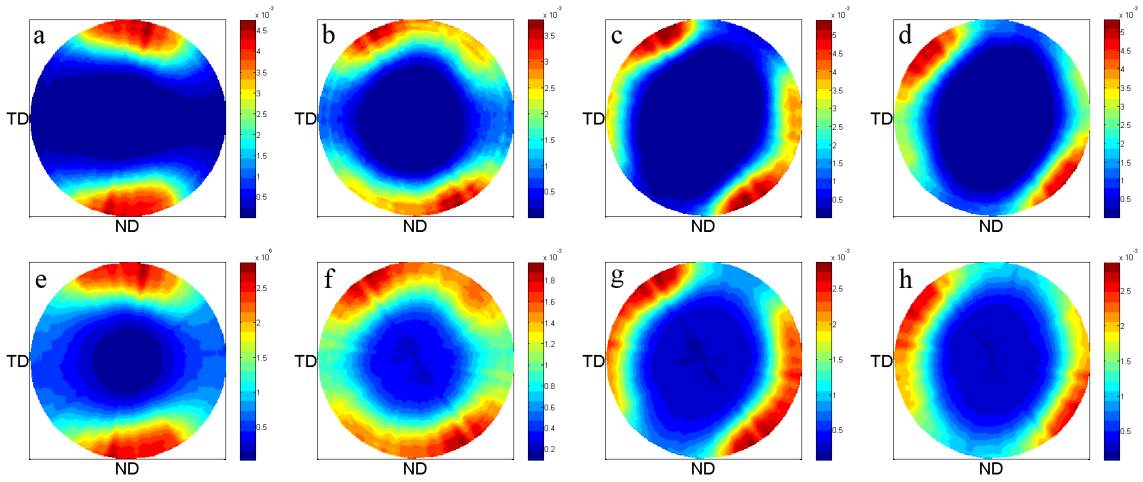

Figure 4.17: Comparison of texture evolution with strain using the intercalated peak (top row) and phase separated peak (bottom row). a/e) The original compressed disc sample, with no strain. Strains of b/f) 0.32 c/g) 0.52 and d/h) 0.60

Comparison of texture evolution across a sample

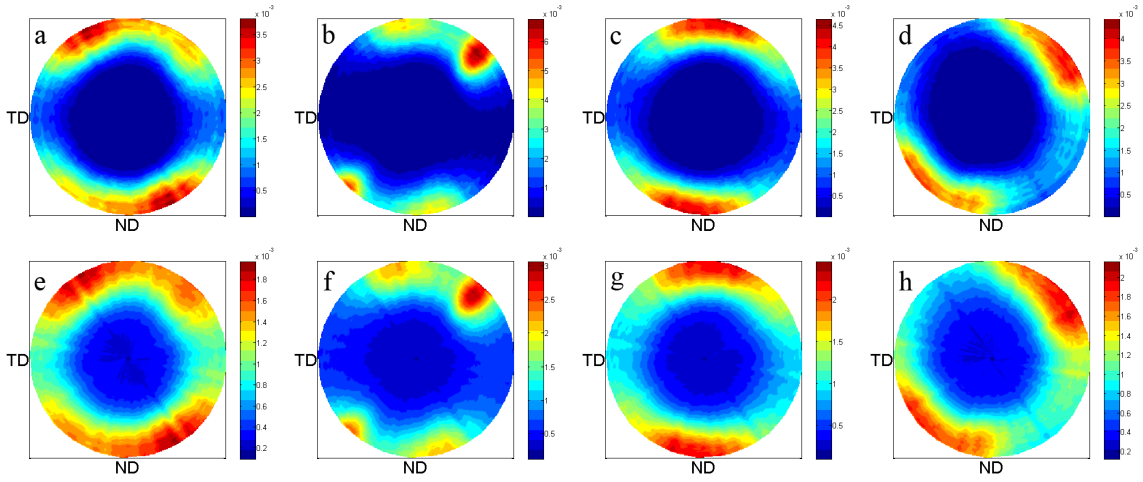

Figure 4.18: Comparison of texture evolution across a sample using the phase separated peak (top row) and intercalated peak (bottom row). Figures a-d and e-h represent the four sections of the sample which were cut after deformation with a and e corresponding to the first section, b and f the second, c and g the third, and d and h the fourth.

Figure 4.18 illustrates how texture evolves across a sample. The top row pole

figures were created using the phase separated XRD peak, while the bottom row pole figures were created using the intercalated XRD peak. An obvious difference is seen: the pole in the intercalated phase are more dispersed than those in the phase separated phase. Figure 4.18a and Figure 4.18e do show slightly more difference than the others. Figure 4.18e has a more symmetrical contour than that of its phase separated counterpart in Figure 4.18a. These differences would go unnoticed without the innovative technique presented here. These microstructural features could potentially play a significant role in property manipulation and can now be examined.

4.4.5 Combinatorial Effects

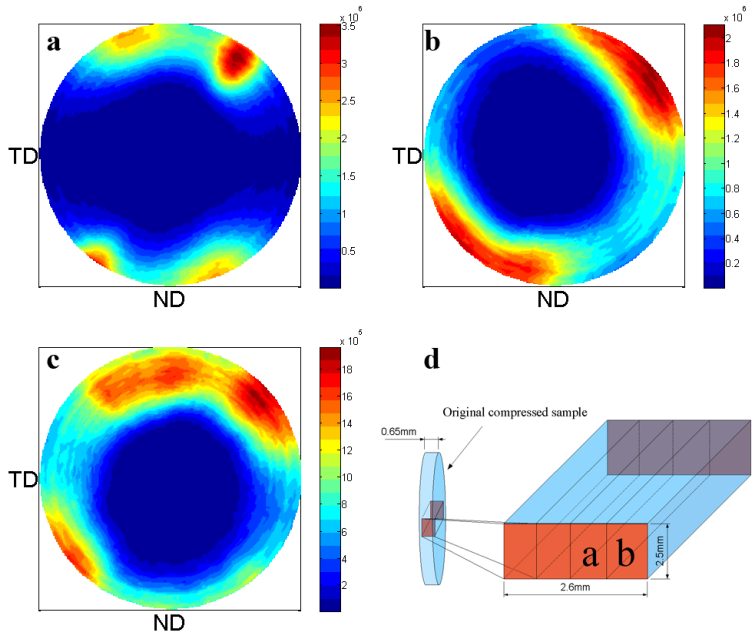

Figure 4.19: Combinatorial effects of the XRD pole figure texture analysis technique

Two samples were cut from a reprocessed sample of 5wt% 25A composite. Figure 4.19d illustrates the location from which the two sections were taken. These

two sections are represented by their respective pole figures in Figures 4.19a-b.

The pole figure represented in Figure 4.19c was created from the combined **a** and **b** sections of the sample. Before they were separated, XRD patterns for the combined sample were collected in the same manner all of the other XRD patterns were collected in this report. If the technique works correctly, an averaging of the two pole figures should produce the combined pole figure. It is not precisely an average of the two, and this could be for a couple of reasons:

- While considerable care was taken to make sure the beam traveled through the center of the sample as it rotated, the beam might not have traveled through the same vertical location. Considerable heterogeneity was seen throughout the thickness of the sample, and the same could be true in the vertical dimension.

- Because the combined sample was of larger dimensions than the other two and a separate volumetric correction factor was not calculated for the new geometry, volumetric attenuation effects could distort the pole figure.

General features are visible, however, including the primary plate normal concentration to the northeast and southwest, as well as the secondary halo to the northwest.

Chapter 5: Conclusions

The purpose of this study was to develop an innovative technique to study the microstructure of polymer-clay nanocomposites. Current microstructure descriptors such as volume or weight fraction, morphology, or uniaxial or biaxial orientation factors are the beginning of microstructure characterization, but to develop more rigorous structure-property relations more information is needed. Anisotropic material properties cannot be avoided nor should they be ignored or marginalized. The next step is an orientation distribution of the reinforcing phase.

An X-ray diffraction technique was presented which allowed non-destructive evaluation of orientation distribution of clay plates in polystyrene with two different morphologies: intercalated and phase separated. Intercalated samples showed increases in mechanical properties and were confirmed intercalated by XRD. Thermal properties for all composite samples improved compared with pure polystyrene. Light absorption increased with the loading of nanoclay.

The surfactant modifier in the clay affected orientational preference based on hydrophilicity. The more hydrophilic the modifier, the more easily the clay plates moved under deformation and the plate normals converged. Deformed sample textures were compared at different strains. When the compression axis lay in the same plane as the clay plates, they shifted toward the perpendicular direction.

Texture changed as a function of position in the sample as well, and this was documented with the new technique. It was also shown that intercalated plates are more difficult to move than phase separated ones and therefore the distribution of plate normals garnered from intercalated peaks of mixed sample or from intercalated samples shows greater breadth.

Bibliography

[1] K. Masenelli-Varlot, E. Reynaud, G. Vigier, and J. Varlet. Mechanical properties of clay-reinforced polyamide. *J. Polym. Sci. B, Polym. Phys. (USA)*, 40(3):272 – 83, 2002/02/01.

[2] Qiang Zheng, Bo Xu, Yihu Song, and Yonggang Shangguan. Calculating barrier properties of polymer/clay nanocomposites: Effects of clay layers. *Polymer (UK)*, 47(8):2904 – 10, 2006/04/05.

[3] Jin Zhu, A.B. Morgan, F.J. Lamelas, and C.A. Wilkie. Fire properties of polystyrene-clay nanocomposites. *Chem. Mater. (USA)*, 13(10):3774 – 80, 2001.

[4] J.L. White and J.E. Spruiell. Specification of biaxial orientation in amorphous and crystalline polymers. *Polymer Engineering and Science*, 21(13):859–868, 9 1981.

[5] Chang Ho Suh and James L. White. Particle and polymer chain orientation development in thermoformed talc-filled thermoplastics. *Polymer Engineering and Science*, 36(17):2188 – 2197, 1996.

[6] A. Ajji, X. Zhang, and S. Elkoun. Biaxial orientation in polyethylene films: Comparison of infrared spectroscopy and x-ray pole figures and birefringence techniques. *Polymer*, 2(46):3838–3846, 2005.

[7] R.J. Pazur, A. Ajji, and R. Prud'homme. X-ray and birefringence orientation measurements on uniaxially deformed polyethylene film. *Polymer (UK)*, 34(19):4004 – 14, 1993/10/.

[8] A. Bafna, G. Beaucage, F. Mirabella, and S. Mehta. 3d hierarchical orientation in polymer-clay nanocomposite films. *Polymer*, 44(4):1103 – 1115, 2003. Compatibilizers;.

[9] D. Li, H. Garmestani, S.R. Kalidindi, and R. Alamo. Crystallographic texture evolution in high-density polyethylene during uniaxial tension. *Polymer (UK)*, 42(11):4903 – 13, 2001/05/.

[10] Marcia C. Branciforti, Lilia M. Guerrini, Rogerio Machado, and Rosario E. S. Bretas. Correlations between processing parameters, morphology, and properties of blown films of lldpe/ldpe blends, part 2: Crystalline and amorphous biaxial orientation by waxd pole figures. *Journal of Applied Polymer Science*, 102(3):2760 – 2767, 2006.

[11] A.K. Taraiya and I.M. Ward. Production and properties of biaxially oriented polyethylene tubes. *Journal of Applied Polymer Science*, 59(4):627 – 638, 1996.

[12] W.E. Dondero and R.E. Gorga. Morphological and mechanical properties of carbon nanotube/polymer composites via melt compounding. *J. Polym. Sci. B, Polym. Phys. (USA)*, 44(5):864 – 78, 2006/03/01.

[13] Z.W. Wilchinsky. Recent developments in measurement of orientation in polymers by x-ray diffraction. *Advances in X-Ray Analysis*, 6:231 – 241, 1963.

[14] G. Brindley and G. Brown. *Crystal structure of clay minerals and their Xray identification*. Mineralogical Society, 1980.

[15] B.K.G Theng. *Formation and Properties of Clay-Polymer Complexes*, volume 9 of *Developments in Soil Science*. Elsevier Scientific Publishing Company, Amsterdam, 1979.

[16] Jae-Hun Yang, Yang-Su Han, Jin-Ho Choy, and Hiroshi Tateyamab. Intercalation of alkylammonium cations into expandable fluorine mica and its application for the evaluation of heterogeneous charge distribution. *The Royal Society of Chemistry*, 11:1305–1312, February 2001.

[17] E.P. Giannelis, R. Krishnamoorti, and E. Manias. *Polymer-silicate nanocomposites: Model systems for confined polymers and polymer brushes*, volume 138 of *Advances in Polymer Science*. Springer Verlag, Berlin, 1999.

[18] Michael Alexandre and Philippe Dubois. Polymer-layered silicate nanocomposites: Preparation, properties and uses of a new class of materials. *Materials Science and Engineering: R: Reports*, 28(1-2):1 – 63, 2000.

[19] H. Fong, W. Liu, C.-S. Wang, and R.A. Vaia. Generation of electrospun fibers of nylon 6 and nylon 6-montmorillonite nanocomposite. *Polymer*, 43(3):775 – 780, 2002.

[20] Maged A. Osman, Michael Ploetze, and Peter Skrabal. Structure and properties of alkylammonium monolayers self-assembled on montmorillonite platelets. *Journal of Physical Chemistry B*, 108(8):2580 – 2588, 2004.

[21] Yulia Lyatskaya and Anna C. Balazs. Modeling the phase behavior of polymer-clay composites. *Macromolecules*, 31(19):6676 – 6680, 1998.

[22] S. Takahashi, M. Taniguchi, K. Omote, N. Wakabayashi, R. Tanaka, and A. Yamagishi. First observation of in-plane x-ray diffraction arising from a single layered inorganic compound film by a grazing incidence x-ray diffraction system with a conventional laboratory x-ray source. *Chem. Phys. Lett. (Netherlands)*, 352(3-4):213 – 19, 2002/01/30.

[23] Hendrik Heinz and Ulrich W. Suter. Surface structure of organoclays. *Angewandte Chemie - International Edition*, 43(17):2239 – 2243, 2004.

[24] Richard A. Vaia and Emmanuel P. Giannelis. Lattice model of polymer melt intercalation in organically-modified layered silicates. *Macromolecules*, 30(25):7990 – 7999, 1997.

[25] S.C. Tjong. Structural and mechanical properties of polymer nanocomposites. *Materials Science and Engineering R: Reports*, 53(3-4):73 – 197, 2006.

[26] Jui-Ming Yeh, Shir-Joe Liou, Chih-Guang Lin, Yen-Po Chang, Yuan-Hsiang Yu, and Chi-Feng Cheng. Effective enhancement of anticorrosive properties of polystyrene by polystyrene-clay nanocomposite materials. *Journal of Applied Polymer Science*, 92(3):1970 – 1976, 2004.

[27] X. Fu and S. Qutubuddin. Polymer-clay nanocomposites: Exfoliation of organophilic montmorillonite nanolayers in polystyrene. *Polymer*, 42(2):807 – 813, 2001.

[28] Alexander B. Morgan and Jeffrey W. Gilman. Characterization of polymer-layered silicate (clay) nanocomposites by transmission electron microscopy and x-ray diffraction: A comparative study. *Journal of Applied Polymer Science*, 87(8):1329 – 1338, 2003.

[29] Richard A. Vaia, Klaus D. Jandt, Edward J. Kramer, and Emmanuel P. Giannelis. Kinetics of polymer melt intercalation. *Macromolecules*, 28(24):8080 – 8085, 1995.

[30] D.F. Eckel, M.P. Balogh, P.D. Fasulo, and W.R. Rodgers. Assessing organo-clay dispersion in polymer nanocomposites. *J. Appl. Polym. Sci. (USA)*, 93(3):1110 – 17, 2004/08/05.

[31] Michael Sandiford. Stereographic projection. http://jaeger.earthsci.unimelb.edu.au/msandifo/Teaching/Mineralogy2/, April 2006.

Appendix A: Pole Figure MATLAB Code

```
clear;

directory = 'Z:\Masters\XRD_Data\Results\30B0.02--T1--1';
base = '30B0.02--06.19.07--1';

tic
cd(directory);
start_image = 1;
num_images = 72;
iteration = 1;

% Override
original_base = base(4:7);
new_base = original_base; %#ok<NASGU>
new_base = '0.05';
base(4:7) = new_base;

if strcmp(base(1:3),'30B')
    if strcmp(base(4:7),'0.02')
        theta = 0.04133 .* ones(180,1);
        image_dim = 399;
        BG = imread('F:\Masters\Images\Background--...
small_inverted_edited_intercalated.jpg');
    else
        theta = 0.08343 .* ones(180,1);
        image_dim = 699;
        BG = imread('F:\Masters\Images\Background--...
small_inverted_edited.jpg');
    end
elseif strcmp(base(1:3),'25A')
    if strcmp(base(4:7),'0.02')
        theta = 0.04133 .* ones(180,1);
        image_dim = 399;
        BG = imread('F:\Masters\Images\Background--...
small_inverted_edited_intercalated.jpg');
```

```
    else
        theta = 0.08308 .* ones(180,1);
        image_dim = 699;
        BG = imread('F:\Masters\Images\Background--...
small_inverted_edited.jpg');
    end
elseif strcmp(base(1:3),'Na+')
    if strcmp(base(4:7),'0.02')
        theta = 0.04133 .* ones(180,1);
        image_dim = 399;
        BG = imread('F:\Masters\Images\Background--...
small_inverted_edited_intercalated.jpg');
    else
        theta = 0.13195 .* ones(180,1);
        image_dim = 699;
        BG = imread('F:\Masters\Images\Background--...
small_inverted_edited.jpg');
    end
elseif strcmp(base(1:2),'PS')
    theta = 0.16923 .* ones(180,1);
    image_dim = 1699;
    BG = imread('F:\Masters\Images\Background--...
PS_Vol_Correction.jpg');
end

num_images_str = int2str(num_images);
center = [1495.4 1506.0];
polefig_dim = 250;
firstrun = 1;
polefig = zeros(180*num_images,8);
h = waitbar(0,['0/', num_images_str, ' images processed']);
load 'Z:\Masters\XRD_Data\Extra_Data\correction_factor.mat';...
%volume correction
chi = (0:179)' .* (pi/180) + (pi/2); %radians

%%
for eta_int = start_image :iteration: (start_image+num_images-1)

    if eta_int < 10; tempstr = '_00'; else tempstr = '_0'; end
    eta_str = int2str(eta_int);
    if strcmp(base(4:7),'0.02')
        base(4:7) = original_base;
        filename = [directory, '\', base, tempstr, eta_str,...
'_small_inverted_edited_intercalated.jpg'];
        base(4:7) = new_base;
```

```
    else
        base(4:7) = original_base;
        filename = [directory, '\', base, tempstr, eta_str,...
'_small_inverted_edited.jpg'];
        base(4:7) = new_base;
    end
    E = imread(filename)-BG;

    volume_correction = correction_factor(eta_int)*ones(size(chi));

    [R,xp] = radon(E,0:179,3);
    Intensity = (R(2,:))' .* volume_correction;

    eta = ((((eta_int*5)-5)+2.5) * (pi/180)) .*...
ones(size(Intensity)); %radians

    alpha = acos(cos(theta).*sin(chi)); %radians
    beta = atan2((-sin(eta).*sin(theta)+cos(eta).*cos(theta).*...
cos(chi)),(-cos(eta).*sin(theta)-sin(eta).*...
cos(theta).*cos(chi))); %radians

    operate_these = find(alpha > (pi/2));
    alpha(operate_these) = pi-alpha(operate_these);
    for ii = 1:size(beta(operate_these))
        if beta(operate_these(ii)) > 0
            beta(operate_these(ii)) = beta(operate_these(ii))-pi;
        else
            beta(operate_these(ii)) = beta(operate_these(ii))+pi;
        end
    end
%%
%     Stereographic Projection
    c = round((sin(alpha)./(1+cos(alpha))).*cos(beta).*...
(polefig_dim./2))+(polefig_dim./2)+1;
    d = round((sin(alpha)./(1+cos(alpha))).*sin(beta).*...
(polefig_dim./2))+(polefig_dim./2)+1;

    if firstrun == 1
        polefig=[c d Intensity alpha beta eta chi theta];
        firstrun = 0; polefig_length = size(polefig,1);
    else
        polefig(polefig_length+1 : polefig_length+size(c,1),:) = ...
[c d Intensity alpha beta eta chi theta];
        polefig_length = size(polefig,1);
    end
```

```
    eta_str2 = int2str(eta_int-start_image+1);
    waitbar((eta_int-start_image+1)/num_images, h,...
[eta_str2,'/',num_images_str,' images processed']);
end

save(['polefig_', directory(29:size(directory,2)) ,'.mat'],'polefig');
close(h);

%% Normalize pole figure
unnormalized_intensity = polefig(:,3);
sin_alpha = sin(polefig(:,4));
integrand = unnormalized_intensity .* sin_alpha;
total_intensity = sum(integrand) .* ones(size(integrand));
normalized_intensity = ((2*pi) .* unnormalized_intensity) ./...
total_intensity;
polefig(:,3) = normalized_intensity;

%% Pcolor plot
figure
X1 = 1:polefig_dim; Y1 = (1:polefig_dim)';
[X1,Y1,Z1] = griddata(polefig(:,1),polefig(:,2),polefig(:,3),...
X1,Y1,'cubic');
pcolor(Z1); shading interp;
colormap(jet(20));
axis equal; xlim([0 polefig_dim]); ylim([0 polefig_dim]); colorbar;
set(gca, 'XTick',[],'YTick',[]);
text(0,125,'TD','horizontalAlignment','right','verticalAlignment'...
,'middle','FontSize',22)
text(125,0,'ND','horizontalAlignment','center','verticalAlignment',...
'top','FontSize',22)

t=toc %#ok<NOPRT>
```